Processing and Application of Ceramics 12 [2] (2018) 164–170
https://doi.org/10.2298/PAC1802164H

Studies of dielectric and electrical transport characteristics of $BaTiO_3$-$BiFeO_3$-$CaSnO_3$ ternary system

Sugato Hajra[1], Sushrisangita Sahoo[2], Twinkle Mishra[3], Pravat Kumar Rout[3,*], Ram Naresh Prasad Choudhary[2]

[1]*Department of Electronics and Instrumentation, Siksha O Anusandhan, Deemed to be University, Bhubaneswar, India*
[2]*Multifunctional and Advance Materials Laboratory, Department of Physics, Siksha O Anusandhan, Deemed to be University, Bhubaneswar, India*
[3]*Department of Electrical and Electronics, Siksha O Anusandhan, Deemed to be University, Bhubaneswar, India*

Received 11 January 2018; Received in revised form 13 May 2018; Received in revised form 17 May 2018; Accepted 29 May 2018

Abstract

In the present paper, the ternary system 0.90 $BaTiO_3$-0.07 $BiFeO_3$-0.03 $CaSnO_3$ (referred as BTO-BFO-CSO-3) near the morphotropic phase boundary (MPB) was synthesized via a cost effective mixed-oxide route and sintered at 1050 °C. Phase composition analysis confirms that the sample crystallizes in orthorhombic phase with few impurity peaks. Room temperature Raman spectrum depicts the phonon peaks characteristic for BTO-BFO-CSO-3 structure. Microstructural examination by scanning electron microscope shows the uniform distribution of grains on the surface of the density sample. The capacitive and resistive properties at different frequencies and temperatures were obtained by modulus and impedance spectroscopy. The non-Debye relaxation mechanism is highlighted by the impedance analysis. The electrical properties associated with the impedance of the prepared sample are found to be dependent on temperature and frequency. The transport properties follow the Arrhenius equation and the activation energy is calculated for the sample.

Keywords: *solid state reaction, XRD, Raman, conductivity, dielectric properties*

I. Introduction

For the past decades, there is a quest for finding materials having strong magneto-electric properties for microelectronic devices [1,2]. Multiferroics have a unique combination of both ferroelectric as well as ferromagnetic ordering and magneto-electric effect [3]. The electric charges of electrons and ions are responsible for the charge effect, and magnetic properties are governed by spins of electrons. Such characteristics can be implemented in the development of magnetic data storage, phase shifters, sensors, transducers, optoelectronic devices, etc. [4–6]. Among a wide range of multiferroics family, $BiFeO_3$ (BFO) is a distinguished candidate for multifunctional applications due to the existence of multiferroicity in a wide temperature range (i.e., the temperature 1100 K corresponds to ferroelectric phase transition and magnetic transition is near 650 K). BFO has a rhombohedrally-distorted perovskite structure with space group *R*3*c* [7]. A weak ferromagnetic moment exists due to Dzyaloshinskii-Morya interaction which also causes canted anti-ferromagnetic ordering of spins [8,9]. There are some limitations of BFO, like high leakage current, low dielectric constant and high tangent loss, which prevent the material to be used for devices [10]. With respect to $BiMnO_3$, $YMnO_3$, $TbMnO_3$ and $HoMn_2O_5$ multiferroics, the performance of BFO is not satisfactory. Vegas *et al.* [11] reported that $CaSnO_3$ (alkaline earth stannate) has distorted perovskite structure. Kumar *et al.* [12] reported that a $BiFeO_3$-$BaTiO_3$ solid solution exhibits characteristic temperature corresponding to mag-

* Corresponding author: tel: +91 9337261952,
e-mail: *sugatofl@outlook.com*

netic ordering transition. The Neel temperature (T_N) is reported to decrease with the rise of $BaTiO_3$ content in $BiFeO_3$-$BaTiO_3$ system. $BaTiO_3$ is a perovskite ferroelectric which has paraelectric-ferroelectric phase transition at 120 °C [13]. Some other authors reported that complex electronic systems, such as $BaZr_{0.025}Ti_{0.975}O_3$-$BiFeO_3$, $BiFeO_3$-$NaNbO_3$, $BiFeO_3$-$BaTiO_3$, etc., have extensively been studied to make BFO a reliable base for the fabrication of useful devices [14,15].

It is also difficult to fabricate BFO without impurity phases. Thus, Sosnowska *et al.* [16] showed the presence of $Bi_2Fe_4O_9$ and Tabares-Munoz *et al.* [17] reported an impurity peak of $Bi_{46}Fe_2O_{72}$. It is also advantageous to develop BFO-ABO_3 system to enhance the structural stability. Several reasons are behind addition of CSO (alkaline earth stannates) into the BTO-BFO, such as: i) structural stability (i.e. at high temperature no other symmetry-breaking phase transitions are reported for $CaSnO_3$ and up to its melting point it persists in the orthorhombic *Pnma* symmetry), ii) high reactivity and iii) decreasing the processing temperature.

In the present study, we report microstructure, dielectric and transport characteristics of a new composition in BTO-BFO-CSO ternary system (i.e., 0.90 $BaTiO_3$-0.07 $BiFeO_3$-0.03 $CaSnO_3$). In this context the various resistive, conductive and capacitive measurements of the prepared material are studied deeply.

II. Experimental procedure

0.90 $BaTiO_3$-0.07 $BiFeO_3$-0.03 $CaSnO_3$ ceramic sample (denoted as BTO-BFO-CSO-3) was prepared via a cost effective conventional mixed oxides route. High-purity (>99.9% purity) $BaCO_3$ (M/S Loba Chemie Co), Fe_2O_3 (M/S Loba Chemie Co), Bi_2O_3 (M/S Central Drug House Pvt Ltd), TiO_2 (M/S Loba Chemie Co), SnO_2 (M/S Loba Chemie Co) and $CaCO_3$ (Sigma-Aldrich) powders were mixed in required stoichiometry. To maintain the loss during high temperature processing of the material, 2 wt.% of extra Bi_2O_3 was added to the prepared mixture. The mixture was mechanically ground in agate mortar for about 4 h in air as well as wet (methanol) medium until a fine homogeneous powder mixture was obtained. The fine powder was first fired at several temperatures and then finally calcined at 950 °C for 12 h. The calcined powder was compacted into cylindrically shaped pellets of 10 mm diameter and 1–2 mm height by using a hydraulic press at pressure of 4×10^6 N/m^2. As it was difficult to fabricate pellets with the fine powder, 5 wt.% of polyvinyl alcohol (PVA) solution was blended with the powder before fabricating pellets. The compacted green (as prepared) pellets were heated or sintered in a silicon carbide furnace for 12 h at 1050 °C. The PVA binder was burnt out during ceramics processing at high temperature.

Phase purity and basic structure data of the material were obtained using X-ray diffractometer (Rigaku Smartlab, Japan) with CuKα radiation (λ = 0.15406 nm) in 2θ range 20–80°. The surface morphology or microstructural examination of the sample was carried out using micrograph images from M/s Zeiss EVO 18) scanning electron microscope. Elemental analysis was performed with energy dispersive X-ray spectroscopy (EDS). The room temperature Raman analysis was carried out with the help of STR-500 Micro-Raman spectrometer (Japan). The polished disks are coated on the parallel surface of the disk sample with high-grade silver paste to make the surfaces conducting for electrical measurements. A phase sensitive impedance meter (model PSM 1735, N4L, UK) was used to measure the frequency and temperature dependent dielectric and electrical parameters. The measurement of conductivity, impedance and dielectric measurements were performed in a wide temperature (30–450 °C) and frequency (1–100 kHz) ranges.

III. Results and discussion

3.1. Structure and morphology

X-ray diffraction is used to examine the phase purity of the prepared sample. Figure 1 presents the XRD spectrum of the sintered BTO-BFO-CSO-3 sample at room temperature in a wide 2θ (20–80°) range and scan rate of 3°/min. Based on the good correlation and agreement between observed and calculated magnitude of interplanar distance and Bragg's angle, the crystal system was determined as orthorhombic with few impurity/unknown phase. Most of the peaks were indexed by a commercially available computer software POWD-MULT [18]. Calculated lattice parameters of the orthorhombic cell of the prepared sample are found to be a = 24.148(2) Å, b = 3.915(20) Å, c = 20.080(2) Å. The relative density of the sample was calculated to be 95% TD.

The surface microstructure of the prepared sample is shown in Fig. 2a. The sintering temperature and time, processing atmosphere and compositional variation often have a great influence over the grain density. Dur-

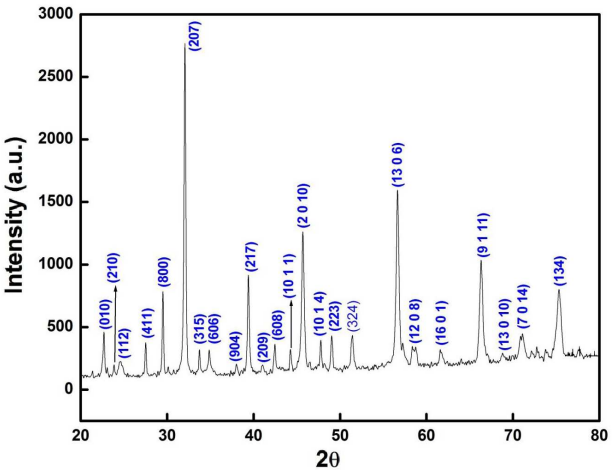

Figure 1. XRD pattern of sintered BFO-BTO-CSO-3

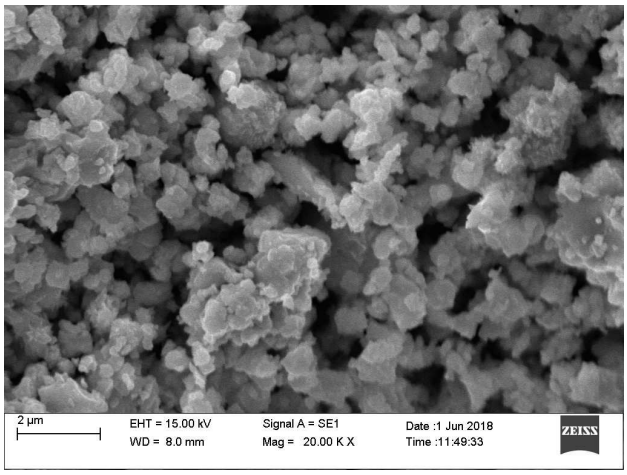

(a)

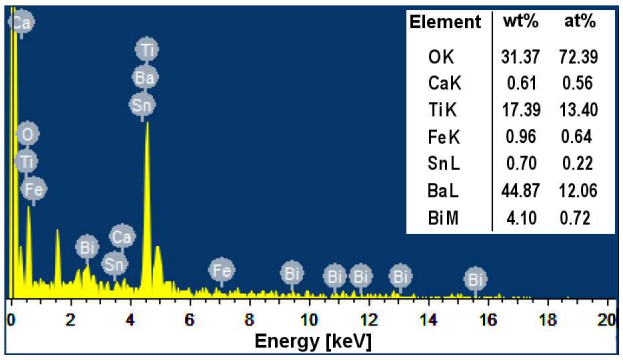

(b)

Figure 2. SEM micrograph (a), EDS spectrum and composition (b) of sintered BFO-BTO-CSO-3

ing the synthesis, sample grain size is governed by thermodynamics of nucleation throughout preparation and it controls unique properties of the materials [19]. The microstructure image shows uniform grain structure without many voids. The chemical composition of the prepared sample was examined by EDS (Fig. 2b). Composition shows the presence of Bi, Ba, Sn, Ca, Fe, Ti, O ions in reasonable amounts. The elemental mapping was also used and confirmed homogeneous element distributions.

3.2. Raman analysis

Figure 3 presents the room temperature Raman spectrum of the BFO-BTO-CSO-3 sample. For an orthorhombic structure (space group *Pnma*) basically the number of unpolarized Raman active modes is approximately half of the polarized ones [20]. Porporati *et al.* [21] reported that Bi contributes in region of lower wave number, i.e. up to 167 cm^{-1}, modes above 262 cm^{-1} are strongly dominated by the oxygen motion and in the region between 152 cm^{-1} and 262 cm^{-1} there is an influence of Fe ions. The band broadening and local lowering of symmetry of Raman spectra is related to BFO substitution due to the local stress and point defects [22]. Raman modes from 175 cm^{-1} to 314 cm^{-1} are related to O–Ti–O bending modes. The high-wave number region

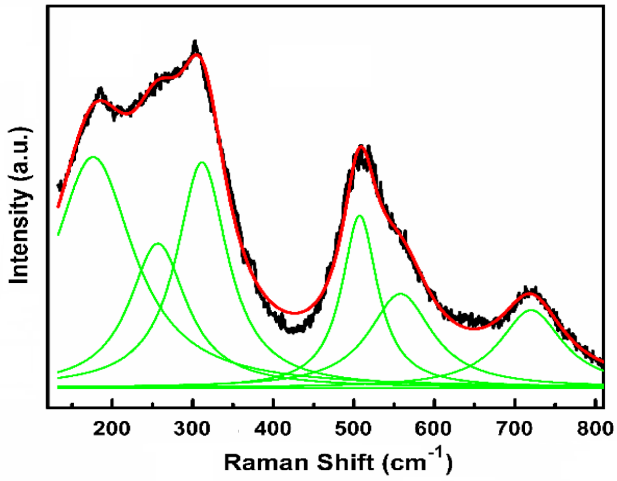

Figure 3. Room temperature Raman analysis of sintered BTO-BFO-CSO-3 sample

vibration (>490 cm^{-1}) confirms the presence of oxygen octahedral. The band near 555 cm^{-1} corresponds to the *E* mode of BFO [23]. The band at 724 cm^{-1} is significantly broader and weak for the paraelectric phase, and reveals unique tetragonal phase. In addition, another mode appears at ~858 cm^{-1} which represents both A-site and B-site substitution which corresponds to the stretching of BO_6 octahedral [24].

3.3. Dielectric study

Figure 4a shows that transition temperature (T_c) basically disappears or moves to higher temperature side for higher frequencies (5 kHz and 10 kHz). There is a hump seen near 30 °C which commonly refers to the depolarization temperature (T_d) which corresponds to transition from ferroelectric state to anti-ferroelectric state. A dielectric anomaly or hump is also observed for 1 kHz at 276 °C which may be due to the point defects generated during sintering in air. The movement of T_c (i.e. transition from antiferroelectric state to paraelectric state) towards high temperature is likely due to the space charge polarization, since diffusion of ions takes place with the increase in temperature. Additionally, thermal energy may also assist in overcoming the activation barrier for the orientation of polar molecules in the direction of the field which increases the dielectric constant [5]. The increase in the value of dielectric loss with temperature is due to the conduction or release of various residual and absorption currents.

Figure 4b presents the frequency dependent dielectric constant and loss factor. It can be seen that with increasing frequency, the value of the dielectric constant falls rapidly, and at higher frequency (>10 kHz) it further merges/coincides for all temperatures. The dipolar and space charge polarization in the low-frequency zone have a major role in the rise of dielectric constant [26]. The ionic and electronic polarizations at higher frequency donate more towards the dielectric constant. In the higher frequency, the sample's net polarization drops as each polarization mechanism (dipolar, space charge,

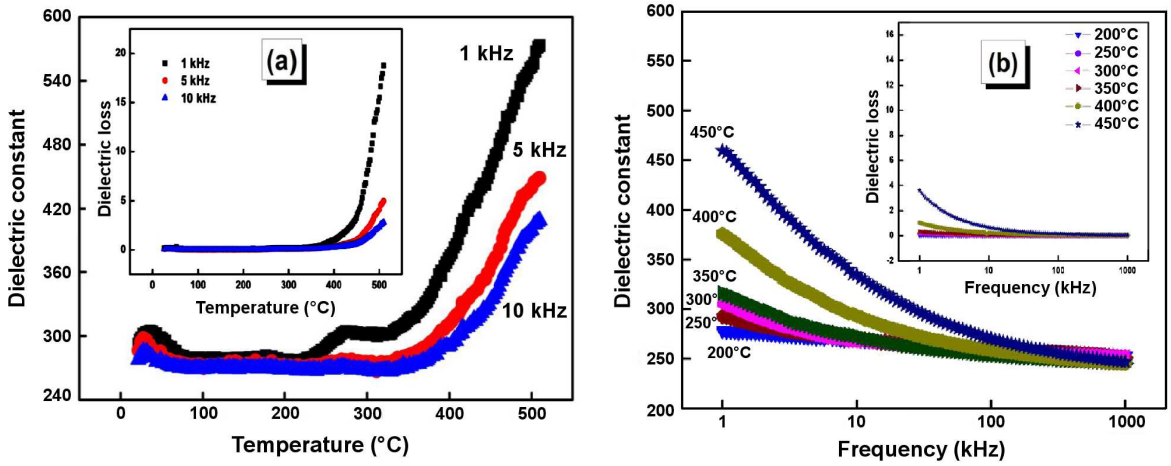

Figure 4. Temperature (a) and frequency (b) dependences of dielectric constant and dielectric loss of BTO-BFO-CSO-3 sample

ionic, electronic) ceases to contribute. So the lower frequency value of dielectric constant is more than that of high frequency [27]. From the frequency dependent dielectric loss, it is seen that the rate of increase of loss is relatively higher in the high-temperature region than in the low-temperature. The fast change in the dielectric loss may be due to the compositional fluctuation, the presence of secondary phase or defects generated during the processing of the sample.

3.4. Impedance

Figure 5a shows the AC field (frequency) dependent Z' of the prepared sample at different temperatures. It reveals that Z' increases with rise in temperature in the low frequency range (up to a certain frequency), and further coincide at high frequencies. The nature of variation of Z' may be due to the release of space charge polarization with increases in frequency and temperature. It is also seen that above a certain frequency, Z' becomes independent of frequency. Figure 5b represents frequency dependent Z'' spectrum. It mainly presents the most resistive behaviour in the prepared sample. The frequency of the applied AC field with respect to Z'' is taken as relaxation. There is a correlation between the imaginary part of impedance and the loss tangent. It is observed that there is no peak in the low temperature region suggesting the lack of dissipation of current in this temperature region. The broadening of peaks with rise in temperature depicts a temperature dependent electrical relaxation process. The relaxation process may be due to the vacancies/defects and immobile charges at high temperature [28]. The frequency dependent Z'' may be symmetric or asymmetric. The symmetric peaks correspond to the Debye relaxation type, whereas the non-Debye type of relaxation gives asymmetric peaks. The asymmetric broadening of peak suggests a spread of relaxation time with two equilibrium positions. Further, it is seen that the value of imaginary part of impedance is reduced with peak shift at higher frequency side and finally merges. This indicates the accumulation of space charge in the material [29].

3.5. Conductivity studies

Conductivity measurements were performed in the context of determining the electrical conduction mechanism which is required to check the transport properties of the material. The conduction mechanism is closely related to the sample microstructure and presence of

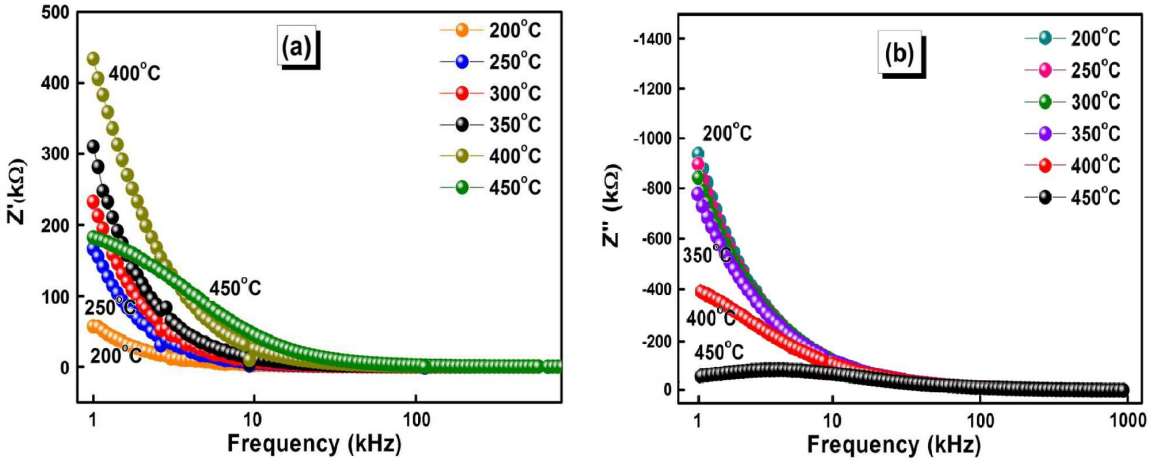

Figure 5. Frequency dependent real (a) and imaginary part (b) of impedance of BTO-BFO-CSO-3 sample

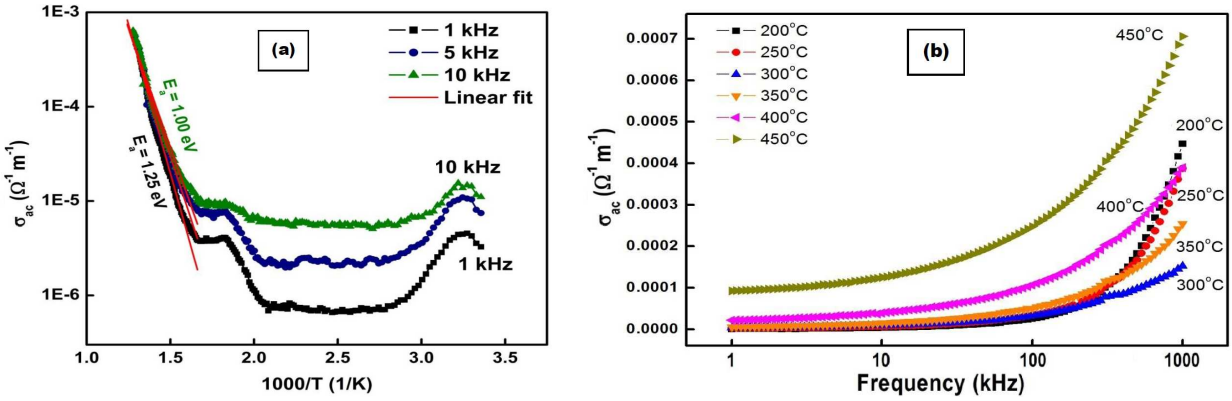

Figure 6. Temperature (a) and frequency (b) dependent AC conductivity of BTO-BFO-CSO-3 sample

various defects. It is well known that material processing conditions (calcination and sintering temperature, time, atmosphere, etc.) generate oxygen and cation vacancies and other defects in perovskites [30].

Figure 6a shows the temperature dependence of AC conductivity from which the activation energy is calculated (from the linear fit). Conductivity variation with temperature can be explained by the following equation:

$$\sigma = \sigma_0 \cdot \exp\left(\frac{-E_a}{k_B \cdot T}\right) \tag{1}$$

where symbols have usual meanings [31,32]. The slopes over a wide temperature region give activation energies. Calculated activation energies for 1, 5 and 10 kHz are 1.00, 1.074 and 1.25 eV, respectively. The slope of Arrhenius equation of conductivity may contain a temperature dependence of mobility as well as enthalpy of reaction to generate free charges. The nature of the deviation of AC conductivity over a temperature variation shows a thermally active material (temperature-dependent model).

Some of the dielectric parameters are used to calculate AC conductivity using the following simple expression:

$$\sigma_{AC} = \omega \cdot \varepsilon_0 \cdot \varepsilon_r \cdot \tan\delta \tag{2}$$

where symbols have their usual meanings. Figure 6b shows frequency dependent electrical conductivity. It is noted that conductance remains constant in the low-frequency region which starts rising on increasing frequency of the applied field. The conductivity pattern obeys Jonscher power law. According to it when a mobile charge carrier jumps to a new position from the old site, it continues in a state of oscillation between two potential energy minima [33].

3.6. Complex electrical modulus

Figure 7a presents the frequency dependent real part of the modulus spectrum at various temperatures (250–450 °C). The value of M' monotonically increases, there is dispersion, and finally at higher frequencies it saturates. The main cause for above behaviour of M' may be the conduction mechanism along with release of short range mobility of charge carriers. On a short range scale, the charges can travel intra- molecularly whereas with increase in the range, the charges will first hope between molecules and further increases in range will lead charges to travel through a number of traps and grain boundaries. With the discharge of the steady electric field, the charge flows with an absence of restoring forces [34]. This depicts the absence of the elec-

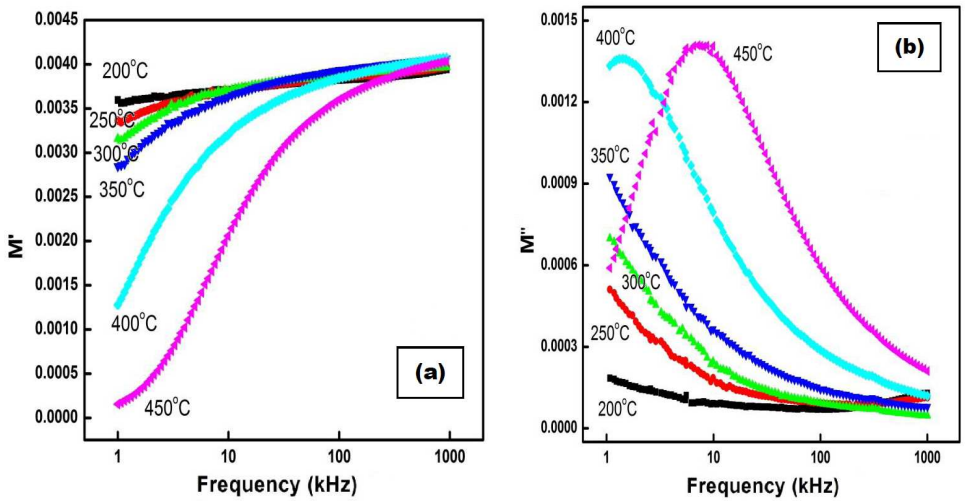

Figure 7. Frequency dependent real (a) and imaginary (b) part of modulus of BTO-BFO-CSO-3 sample

trode effect in the prepared sample. The shift of M'' peak to the high-frequency region is seen in Figure 7b ascribing linkage between the motion of mobile atoms. It shows the thermally activated relaxation mechanism. The asymmetric M'' peak broadening of non-Debye type reveals the spread of relaxation processes with various time constants [35]. The lower frequency peaks suggest that the ions move over a long distance whereas the high frequency peaks coincide with spatially confined ions in their potential well. The modulus plots depict the presence of hopping mechanism for electrical conduction in the prepared sample.

IV. Conclusions

The ternary system of BTO-BFO-CSO-3 is prepared successfully by the cost effective mixed oxide route. The phase analysis from the XRD spectrum shows major orthorhombic phase with few impurity phases. SEM microstructure reveals the high density grain distribution and growth. The homogeneous distribution of composition throughout the sample is confirmed by EDS spectra which is consistent to its base compositions without impurity content. Dielectric analysis shows two phase transitions: T_d and T_c. Modulus analysis shows that non-exponential/non-Debye type of conductivity relaxation is seen in the sample. The high dielectric constant and low tangent loss of the material promise its usage in energy storage devices. On further analysis towards the magneto-electric nature, the prepared sample could have applications in multifunctional device in the future.

Acknowledgements: The authors like to express their sincere thanks to Dr. Kalyani Mohanta, Department of Ceramics Engineering, IIT Banaras Hindu University and Mr. Manojit De GGCU, Bilaspur for their timely help towards SEM and Raman experiment.

References

1. N.A. Spaldin, M. Fiebig, "The renaissance of magnetoelectric multiferroics", *Science*, **309** (2005) 391–392.
2. W. Eerenstein, N.D. Mathur, J.F. Scott, "Multiferroic and magnetoelectric materials", *Nature*, **442** (2006) 759–765.
3. S.-W. Cheong, M. Mostovoy, "Multiferroics: a magnetic twist for ferroelectricity", *Nat. Mater.*, **6** (2007) 13–20.
4. T. Kimura, G. Lawes, A.P. Ramirez, "Electric polarization rotation in a hexaferrite with long-wavelength magnetic structures", *Phys. Rev. Lett.*, **94** (2005) 137201.
5. G. Catalan, J.F. Scott, "Physics and applications of bismuth ferrite", *Adv. Mater.*, **21** (2009) 2463–2485.
6. T. Matsui, H. Tanaka, N. Fujimura, T. Ito, H. Mabuchi, K. Morii, "Structural, dielectric, and magnetic properties of epitaxially grown $BaFeO_3$ thin films on (100) $SrTiO_3$ single-crystal substrates", *Appl. Phys. Lett.*, **81** (2002) 2764–2766.
7. K.F. Wang, J.-M. Liu, Z.F. Ren, "Multiferroicity, the coupling between magnetic and polarization orders", *Adv. Phys.*, **58** (2009) 321–448.
8. C. Ederer, N.A. Spaldin, "Weak ferromagnetism and magnetoelectric coupling in bismuth ferrite", *Phys. Rev. B*, **71** (2005) 060401.
9. C. Michel, J.M. Moreau, G.D. Achenbach, R. Gerson, W.J. James, "Atomic structures of two rhombohedral ferroelectric phases in the $Pb(Zr,Ti)O_3$ solid solution series", *Solid State Commun.*, **7** (1969) 865–868.
10. S.T. Zhang, L.H. Pang, Y. Zhang, M.H. Lu, Y.F. Chen, "Preparation, structures, and multiferroic properties of single phase $Bi_{1-x}La_xFeO_3$ (x = 0-0.40) ceramics", *J. Appl. Phys.*, **100** (2006) 114108.
11. A. Vegas, M. Vallet-Regí, J.M. González-Calbet, M.A. Alario-Franco, "The $ASnO_3$ (A = Ca, Sr) perovskites", *Acta Cryst. B*, **42** (1986) 167–172.
12. M.M. Kumar, S. Srinath, G.S. Kumar, S.V. Suryanarayana, "Spontaneous magnetic moment in $BiFeO_3$-$BaTiO_3$ solid solutions at low temperatures", *J. Magn. Magn. Mater.*, **188** (1998) 203–212.
13. M.B. Smith, K. Page, T. Siegrist, P.L. Redmond, E.C. Walter, R. Seshadri, L.E. Brus, M.L. Steigerwald, "Crystal structure and the paraelectric-to-ferroelectric phase transition of nanoscale $BaTiO_3$", *J. Am. Chem. Soc.*, **130** (2008) 6955–6963.
14. P.A. Jha, P.K. Jha, A.K. Jha, R.K. Dwivedi, "Dielectric behavior of (1-x)$BaZr_{0.025}Ti_{0.975}O_3$-(x)$BiFeO_3$ solid solutions", *Mater. Res. Bul.*, **48** (2013) 101–105.
15. H. Amorin, C. Correas, P. Ramos, T. Hungria, A. Castro, M. Alguero, "Very high remnant polarization and phase-change electromechanical response of $BiFeO_3$-$PbTiO_3$ at the multiferroic morphotropic phase boundary", *J. Appl. Phys.*, **101** (2012) 172908.
16. I. Sosnowska, T.P. Neumaier, E. Steichele, "Spiral magnetic ordering in bismuth ferrite", *J. Phys. C.: Solid State Phys.*, **15** (1982) 4835–4846.
17. C. Tabares-Munoz, J.P. Rivera, A. Benzinges, A. Monnier, H. Schmid, "Measurement of the quadratic magnetoelectric effect on single crystalline $BiFeO_3$", *Jpn. J. Appl. Phys.*, **24** (1985) 1051–1053.
18. E. Wu, POWDMULT: "An interactive powder diffraction data interpretation and indexing program version 2.1", School of Physical Sciences, Flinders University of South Australia, 5042, Australia.
19. M. Sahu, R.N.P. Choudhary, S.K. Das, S. Otta, B.K. Roul, "Inter-grain mediated intrinsic and extrinsic barrier layer network mechanism involved in $CaCu_3Ti_4O_{12}$ bulk ceramic", *J. Mater. Sci.: Mater. Electron.*, **28** (2017) 15676–15684.
20. M.N. Liev, M.V. Abrashev, H.G. Lee, V.N. Popov, Y.Y. Sun, C. Thomsen, R.L. Meng, C.W. Chu, "Raman spectroscopy of orthorhombic perovskitelike $YMnO_3$ and $LaMnO_3$", *Phys. Rev. B*, **57** (1998) 2872–2877.
21. A.A. Porporati, K. Tsuji, M. Valant, A.K. Axelsson, G. Pezzottia, "Raman tensor elements for multiferroic $BiFeO_3$ with rhombohedral *R*3*c* symmetry", *J. Raman Spectrosc.*, **41** (2010) 84–87.
22. J.M.C. Moreno, M. Yoshimura, "Characterization by Raman spectroscopy of solid solutions in the yttria-rich side of the zirconia-yttria system", *Solid State Ionics*, **154-155** (2002) 125–133.
23. D. Kothari, V.R. Reddy, V.G. Sathe, A. Gupta, A. Banerjee, A.M. Awasthi, "Raman scattering study of polycrystalline magnetoelectric $BiFeO_3$", *J. Magn. Magn. Mater.*, **320** (2008) 548–552.
24. S. Hajra, S. Sahoo, T. Mishra, M. De, P.K. Rout, R.N.P. Choudhary, "Studies of structural, dielectric and electri-

cal characteristics of $BaTiO_3$-$BiFeO_3$-$CaSnO_3$ electronic system", *J. Mater. Sci.: Mater. Electron.*, **29** (2018) 7876–7884.
25. A.K. Jonscher, "The 'universal' dielectric response", *Nature*, **267** (1977) 673–679.
26. N. Adhlakha, K.L. Yadav, "Study of dielectric, magnetic and magnetoelectric behavior of (x)NZF-(1-x)PLSZT multiferroic composites", *IEEE Trans. Dielectr. Electr. Insul.*, **21** (2014) 2055–2061.
27. S.A. Mabud, "The morphotropic phase boundary in PZT solid solutions", *J. Appl. Crystallogr.*, **13** (1980) 211–216.
28. P. Sharma, S. Hajra, S. Sahoo, P.K. Rout, R.N.P. Choudhary, "Structural and electrical characteristics of gallium modified PZT ceramics", *Process. Appl. Ceram.*, **11** (2017) 171–176.
29. J.R. Macdonald, "Note on the parameterization of the constant-phase admittance element", *Solid State Ionics*, **13** (1984) 147–149.
30. C.K. Suman, K. Prasad, R.N.P. Choudhary, "Complex impedance studies on tungsten-bronze electroceramic: $Pb_2Bi_3LaTi_5O_{18}$", *J. Mater. Sci.*, **41** (2006) 369–375.
31. S. Sen, R.N.P. Choudhary, "Impedance studies of Sr modified $BaZr_{0.05}Ti_{0.95}O_3$ ceramics", *Mater. Chem. Phys.*, **87** (2004) 256–263.
32. N. Sahu, S. Panigrahi, "Rietveld analysis, dielectric and impedance behaviour of Mn^{3+}/Fe^{3+} ion-modified $Pb(Zr_{0.65}Ti_{0.35})O_3$ perovskite", *Bull. Mater. Sci.*, **36** (2013) 699–708.
33. S. Sahoo, P.K. Mahapatra, R.N.P. Choudhary, M.L. Nandagoswami, A. Kumar, "Structural, electrical and magnetic characteristics of improper multiferroic: $GdFeO_3$", *Mater. Res. Express*, **3** (2016) 065017.
34. R.K. Mishra, D.K. Pradhan, R.N.P. Choudhary, A. Banerjee, "Effect of yttrium on improvement of dielectric properties and magnetic switching behavior in $BiFeO_3$", *J. Phys.: Condensed Matter*, **20** (2008) 04521
35. S. Sahoo, S. Hajra, M. De, R.N.P. Choudhary, "Resistive, capacitive and conducting properties of $Bi_{0.5}Na_{0.5}TiO_3$-$BaTiO_3$ solid solution", *Ceram. Int.*, **44** (2017) 4719–4726.